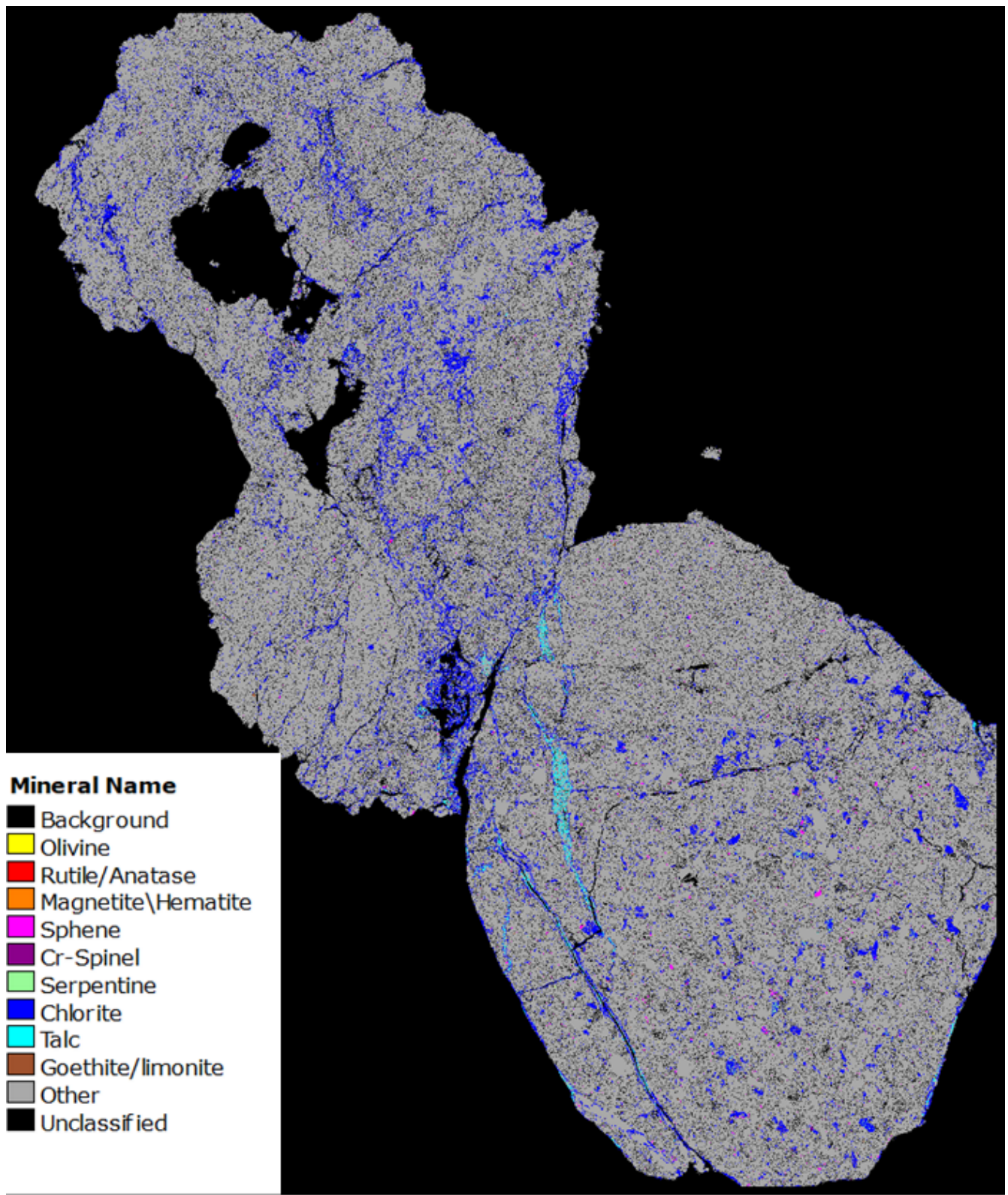


Supporting Information

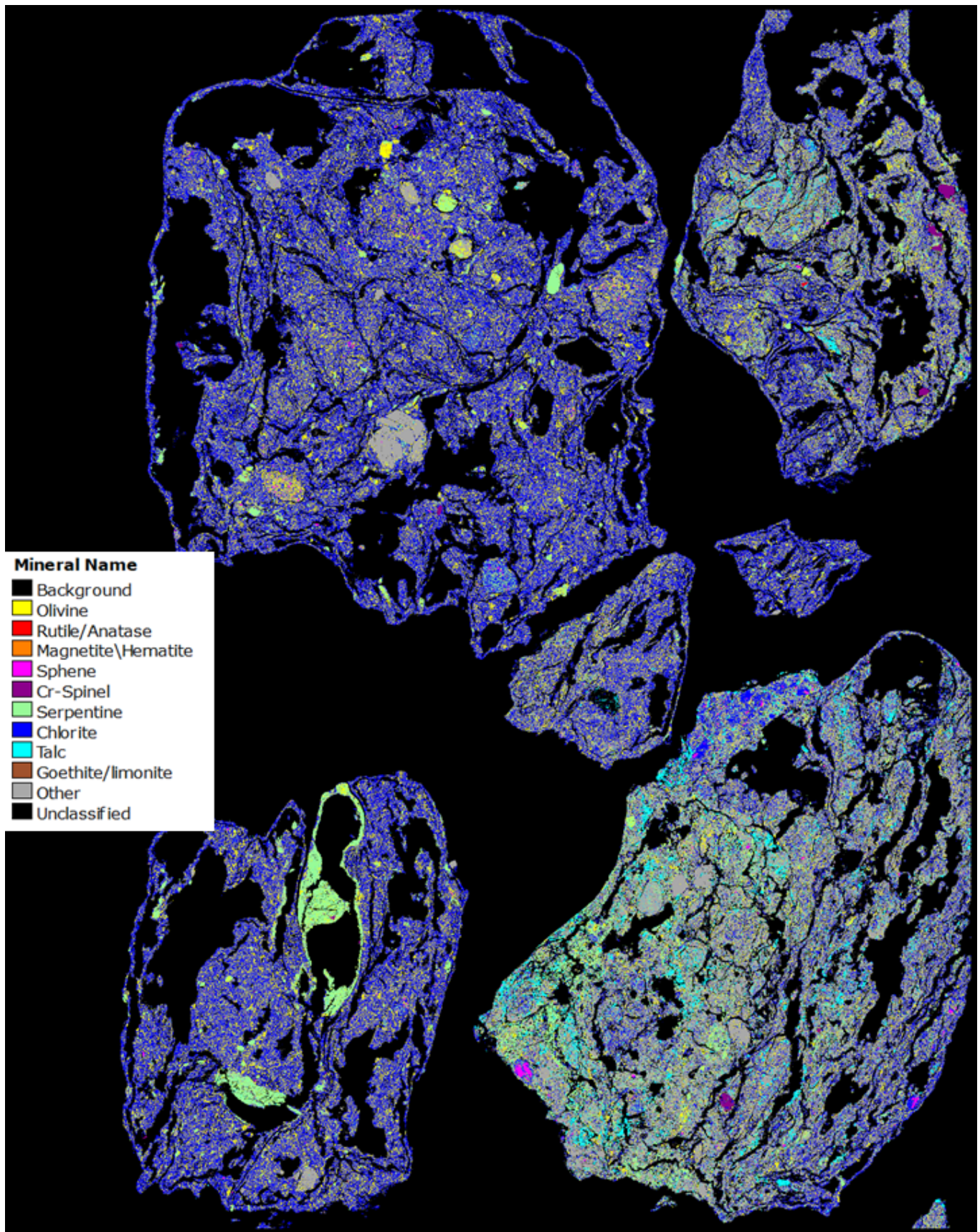
High resolution reproductions of QEMScan results

Reduced Mineral Class Maps

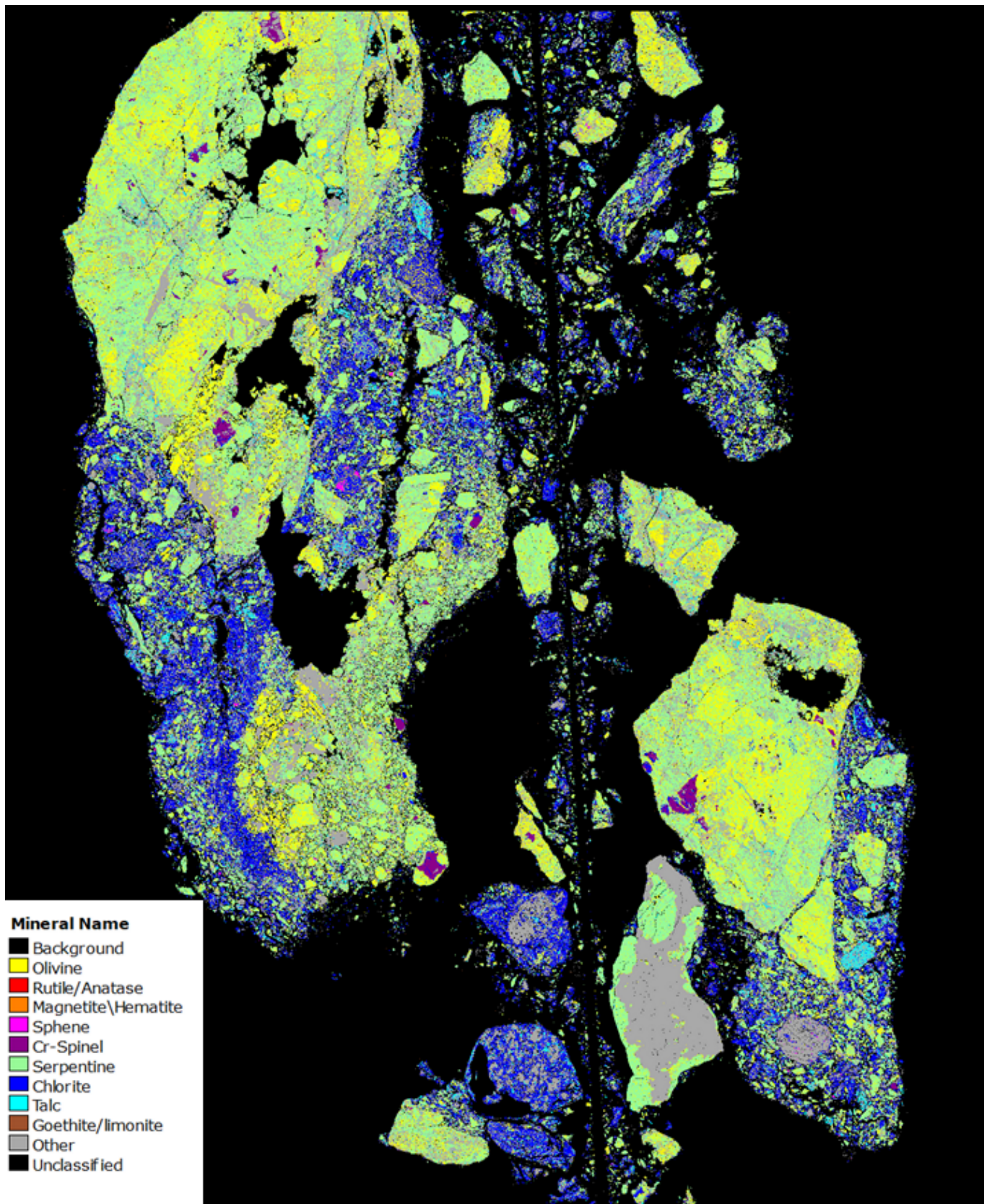
Below we present full page reproductions of the QEMScan datasets presented in Fig 3. Figures S2-S4 show detailed renderings of first column of Fig 3, which details the mineralogy key to understanding the in-situ weathering process. Figure S5 presents a summary bar chart of the phase abundance for this mineral set based on the mineral classifications shown in Table S1.



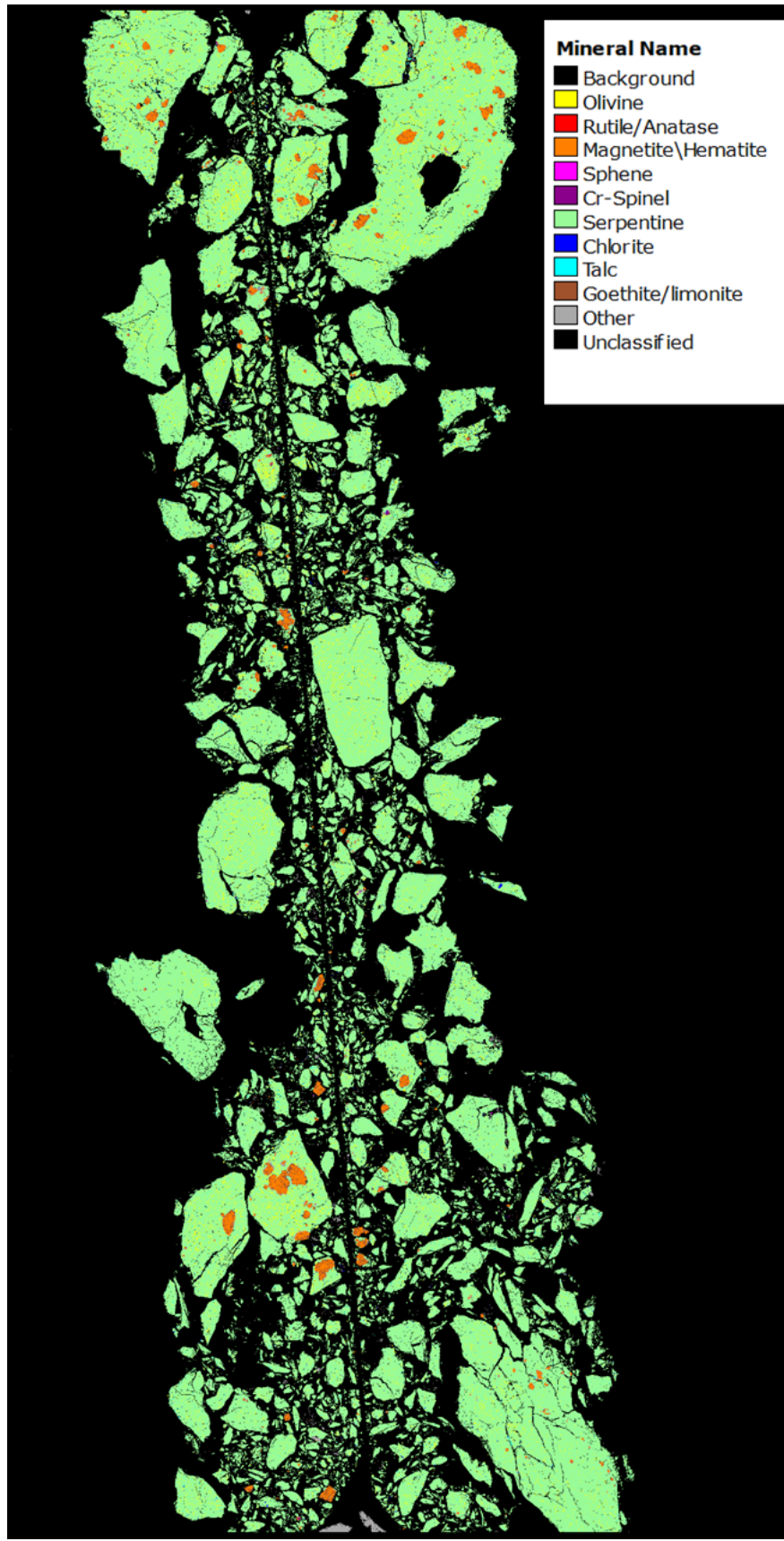
S1 Reduced QEMScan Mineral Phase map QV1.17.



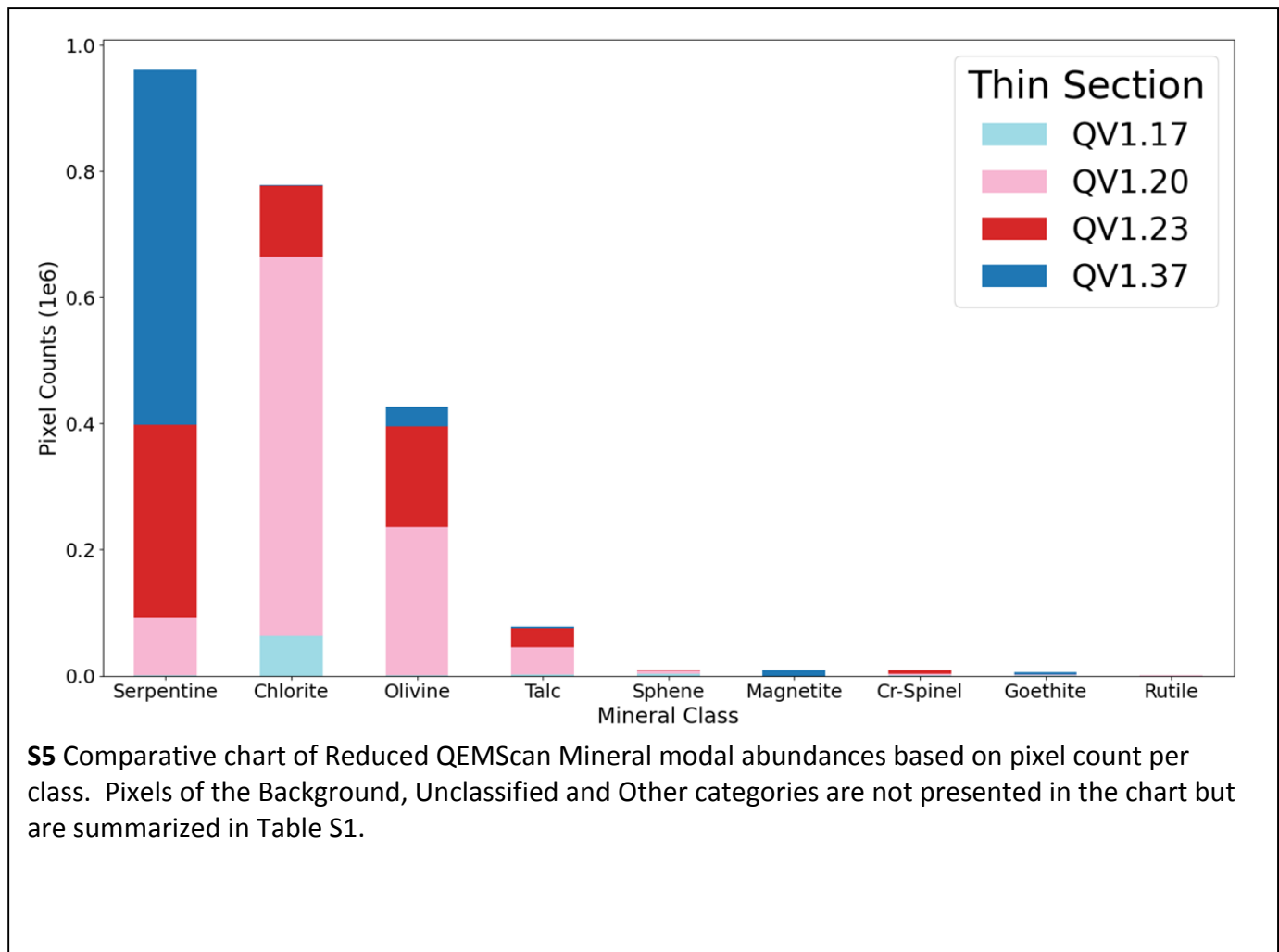
S2 Reduced QEMScan Mineral Phase map of QV1.20.



S3 reduced QEMScan Mineral Phase map of QV1.23.

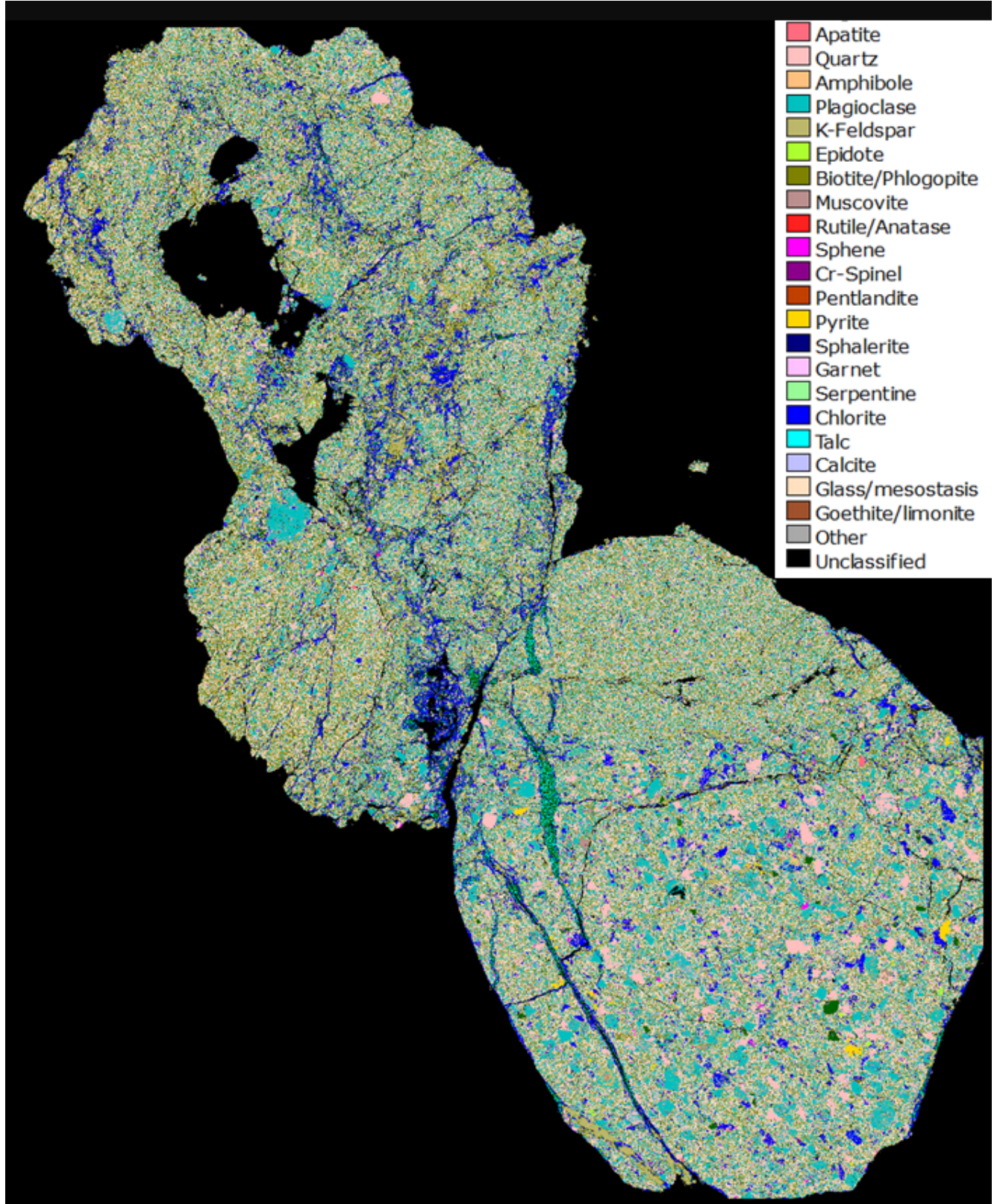


S4 Reduced QEMScan Mineral Phase map of QV1.37.

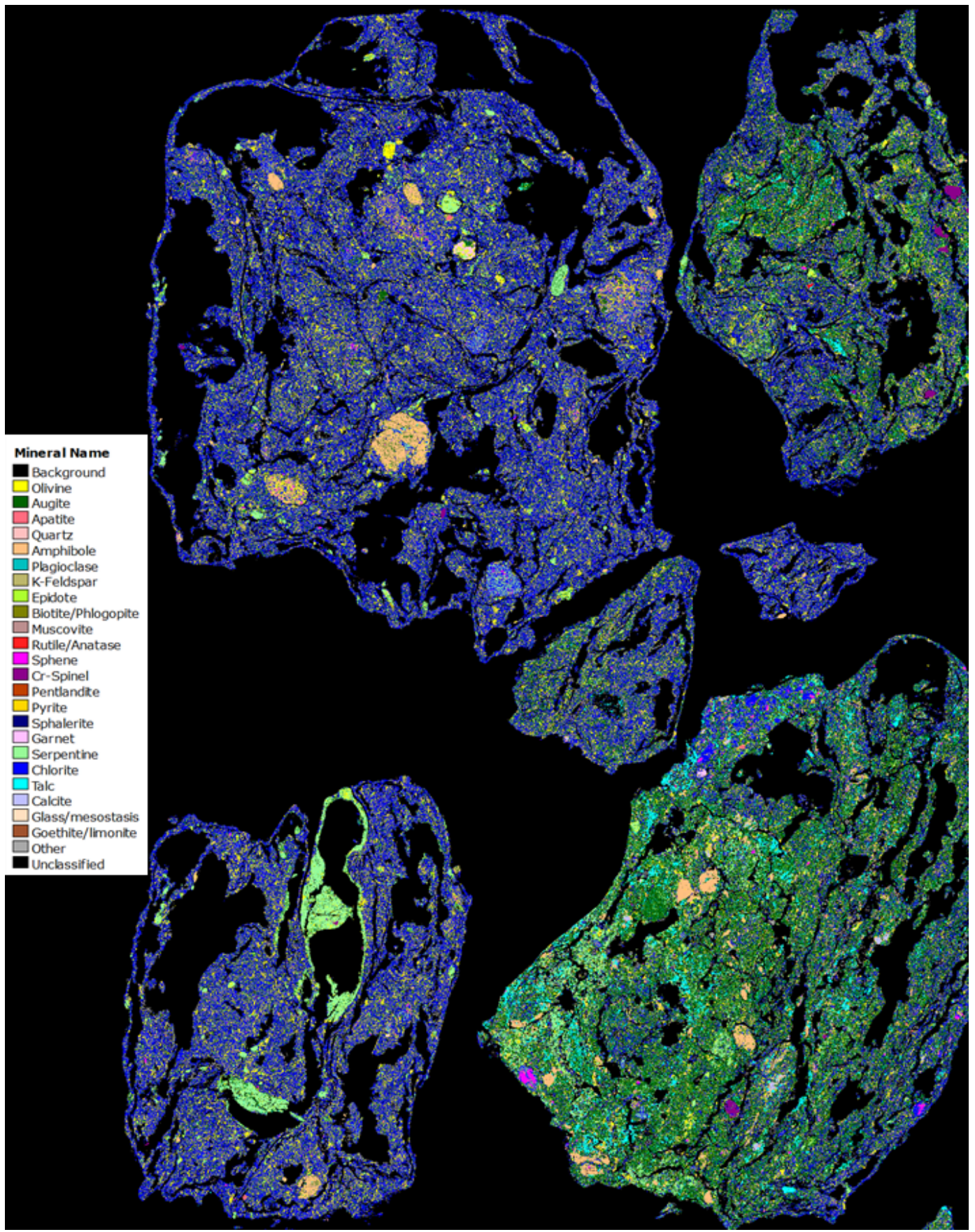


Comprehensive Mineral Maps

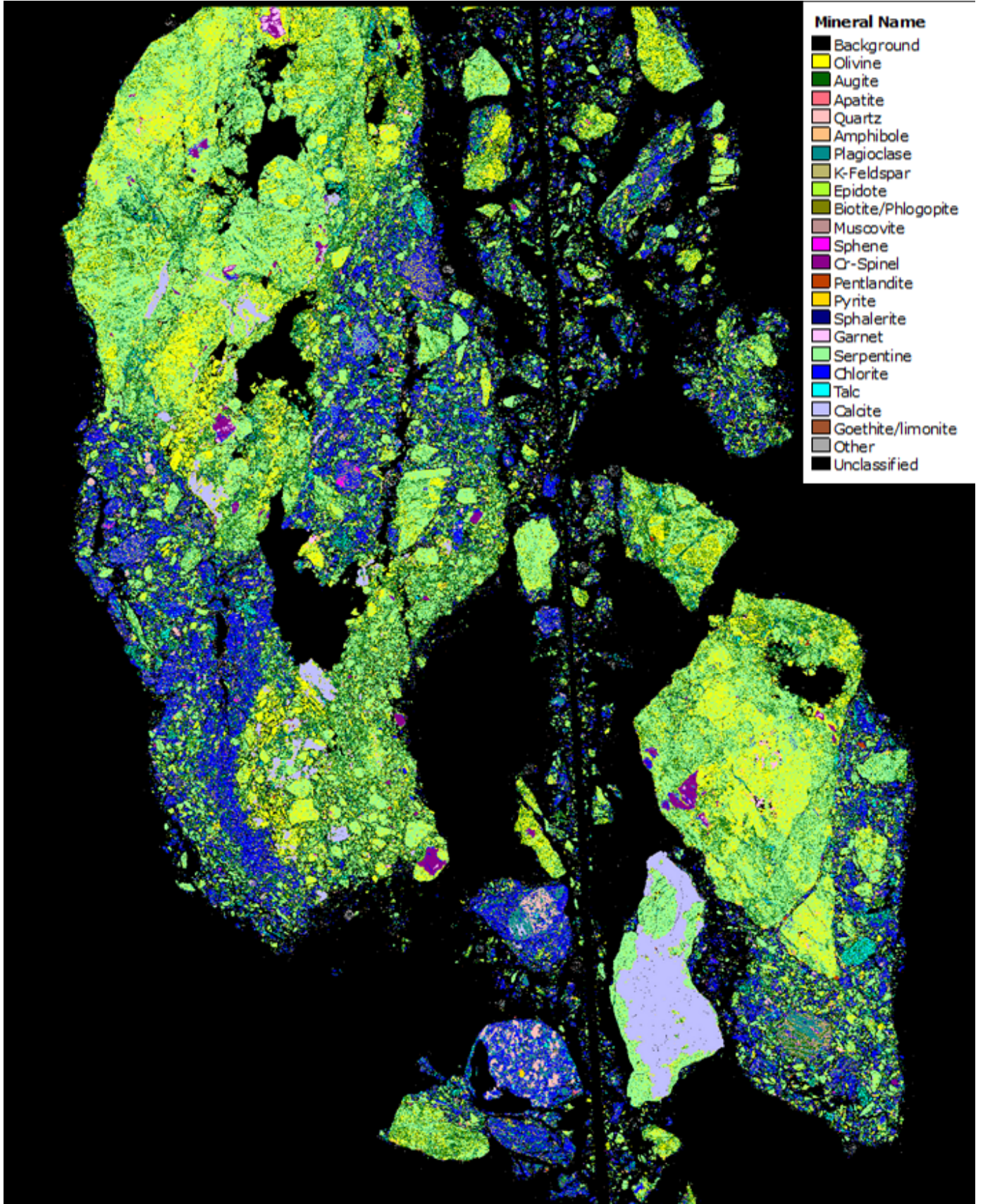
Below we present full page reproductions of the Comprehensive QEMScan Mineral classifications datasets. (Figures S6-S9) We present the Reduced Mineralogy in the manuscript as it is easier to understand the relationships between the phases principally involved in the transport of Fe. Figure S10 presents a summary bar chart of the phase abundance for the mineral classes presented in these maps based on the values summarized in Table S2.



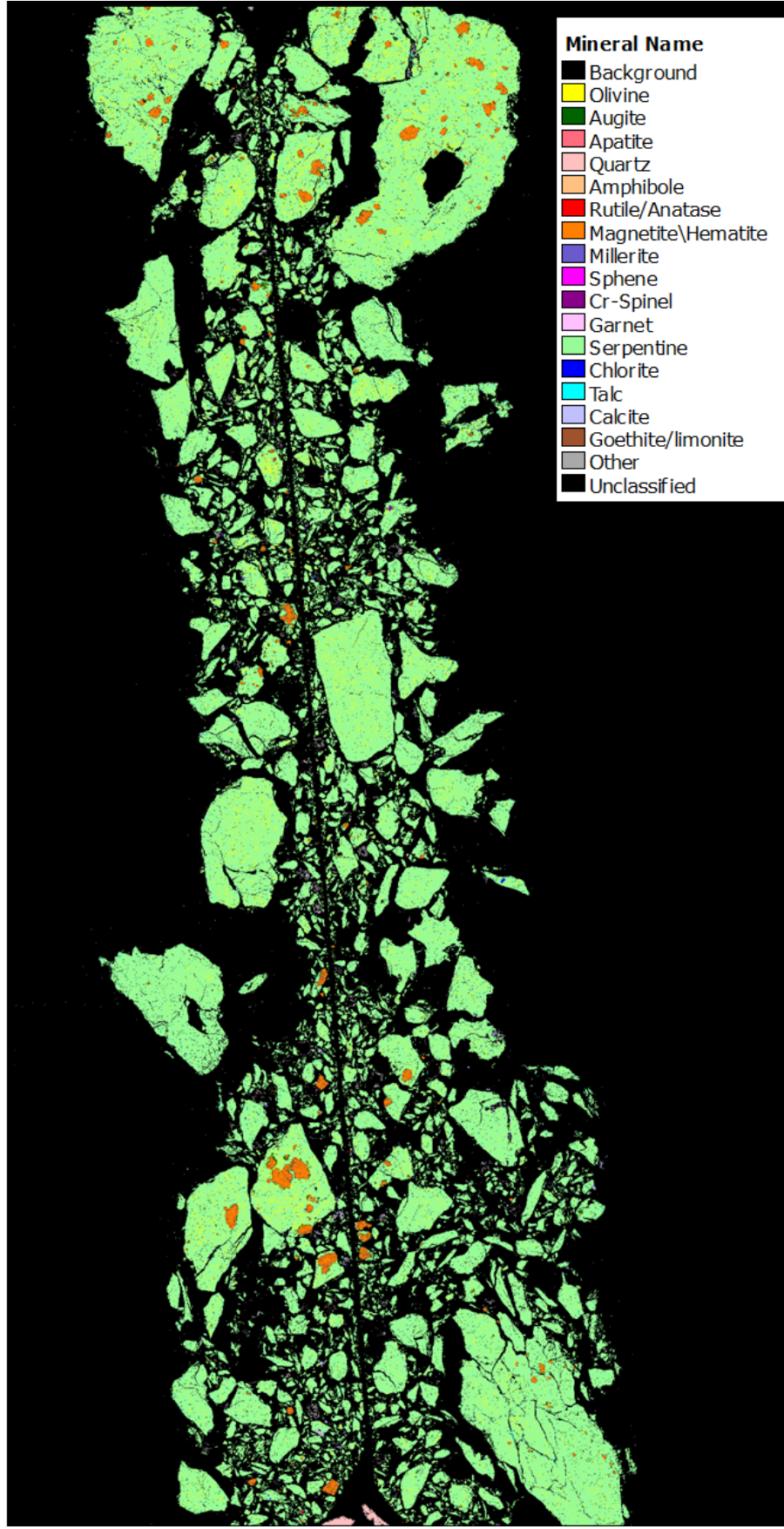
S6 Comprehensive QEMScan Mineral Phase map of QV1.17.



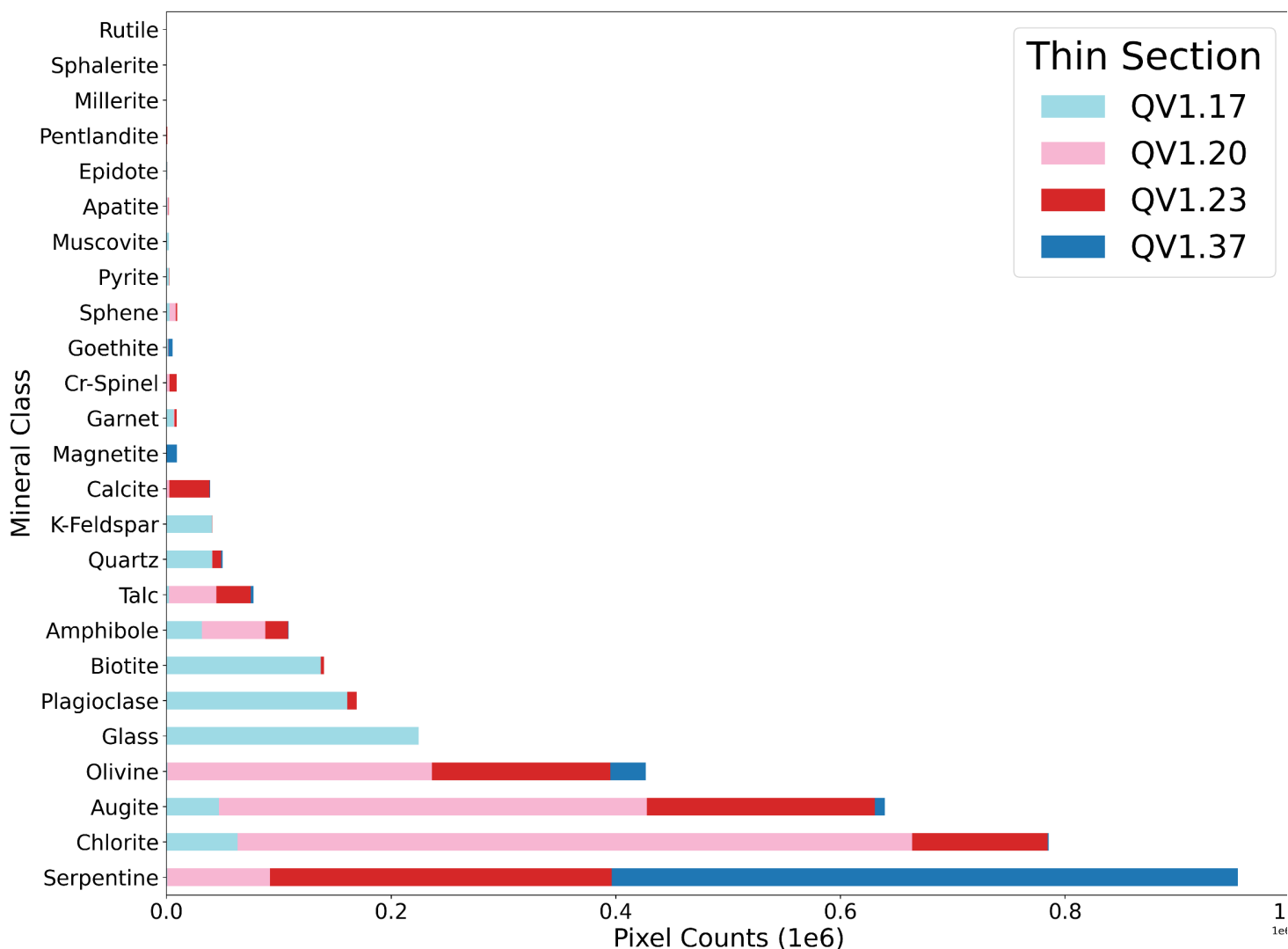
S7 Comprehensive QEMScan Mineral Phase map of QV1.20.



S8 Comprehensive QEMScan Mineral Phase map of QV1.23.



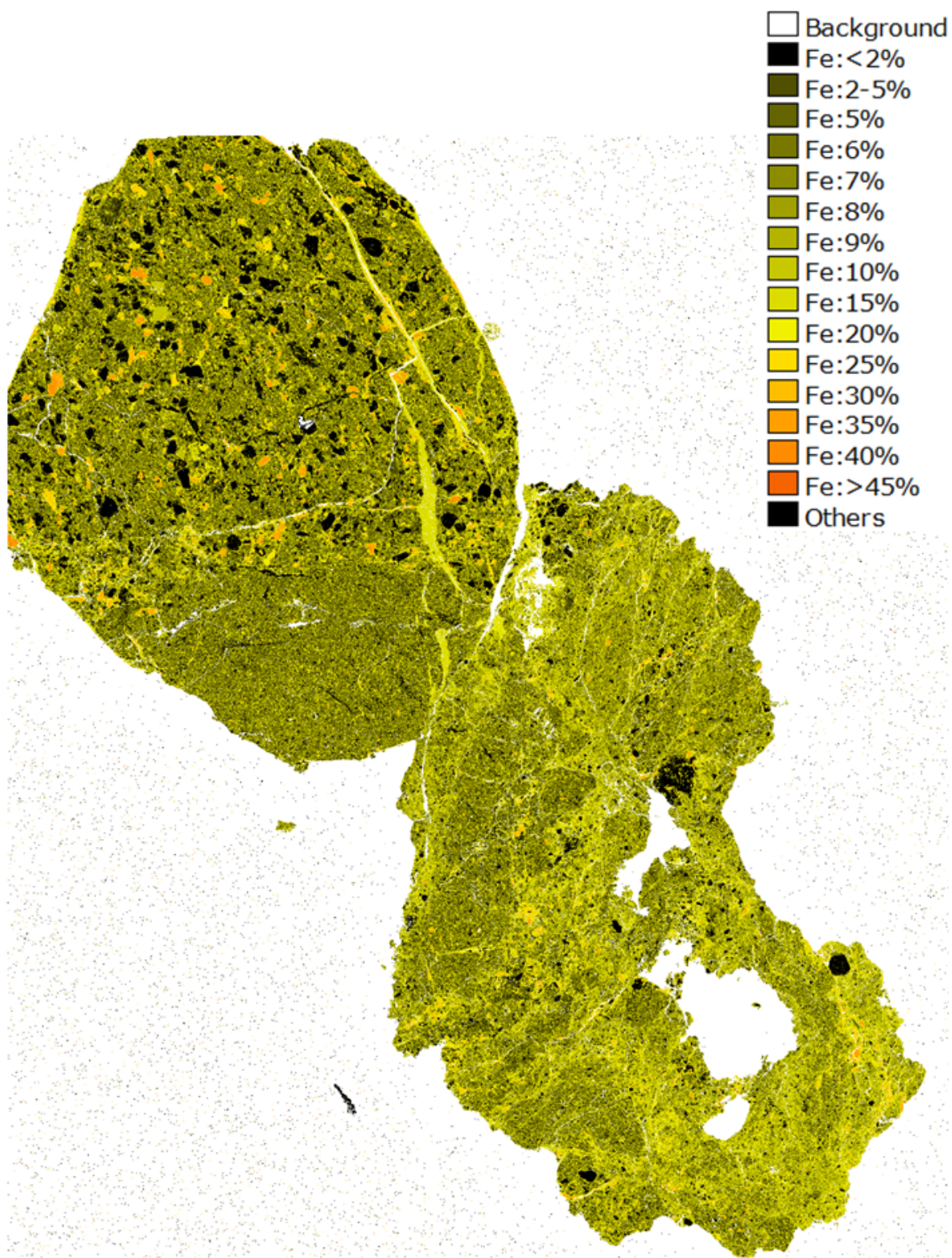
S9 Comprehensive QEMScanning electron micrograph showing mineral phase distribution in sample QV1.37.



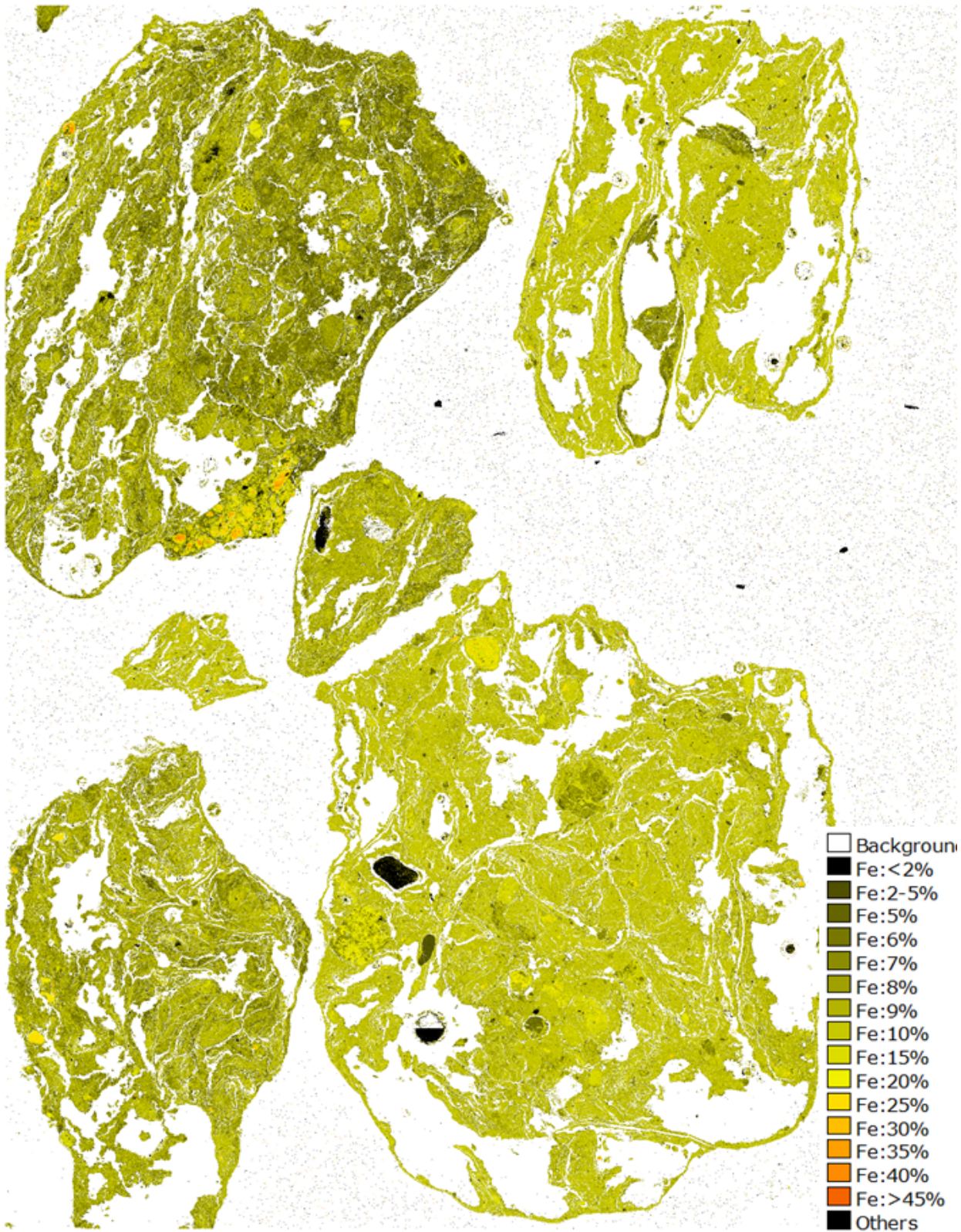
S10 Comparative chart of Comprehensive QEMScan Mineral modal abundances based on pixel count per class. Pixels of the Background, Unclassified and Other categories are not presented in the chart but are summarized in Table S2.

Iron Weight Percent Maps

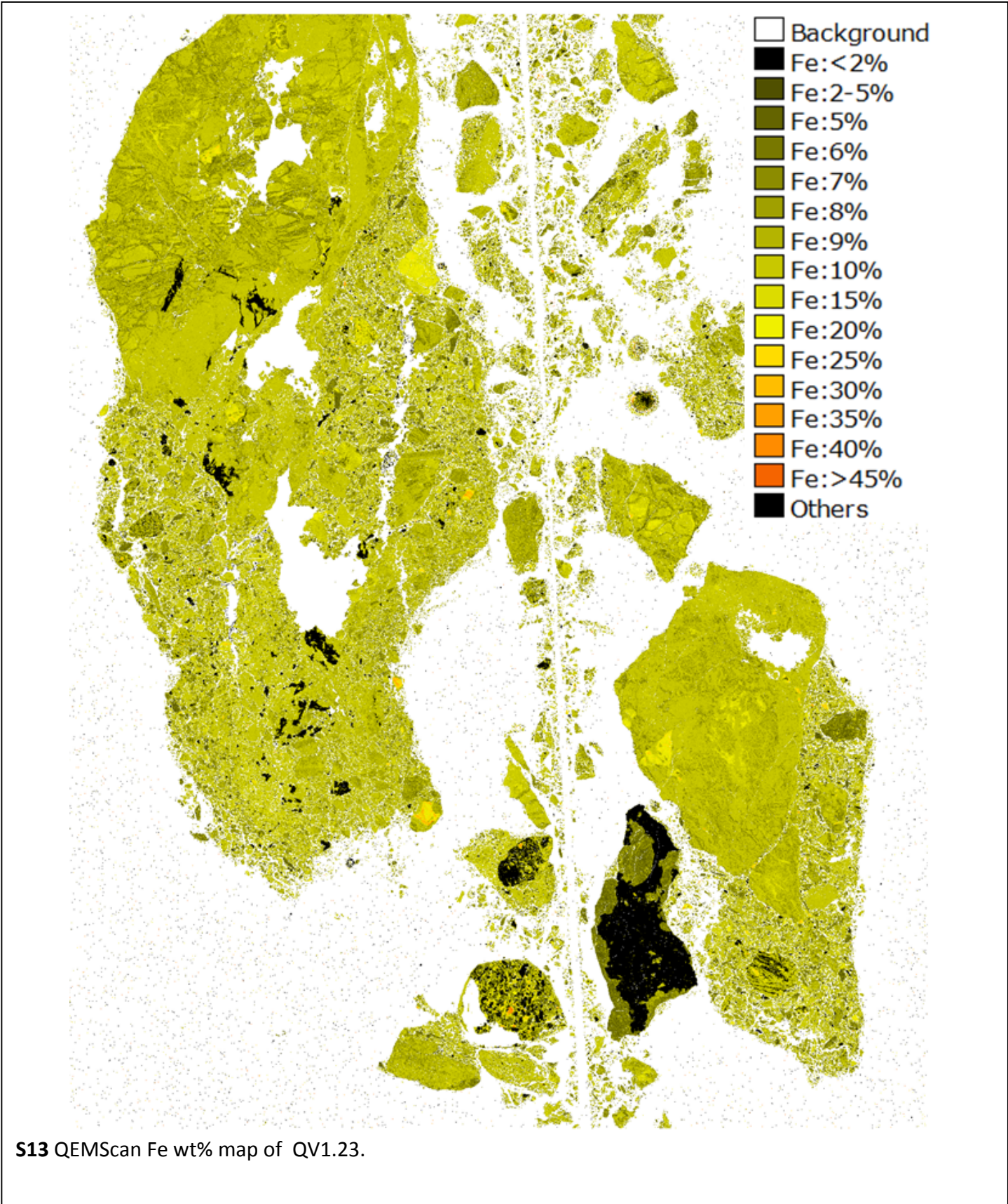
Figures S



S11 QEMScan Fe wt% map of QV1.17.



S12 QEMScan Fe wt% map of QV1.20.



S13 QEMScan Fe wt% map of QV1.23.



Data-driven Microanalysis – Energy Dispersive Spectroscopy and Microstructural Verification

Top down EDS and BSE analysis

The energy dispersive spectroscopic (EDS) map acquired to produce the phase map in Figure 4b, is statistically dense collection of correlated chemical composition measurements. The map consists of 154 by 152 pixels (17 by 21 nm in size) where each pixel records a characteristic x-ray spectrum generated by the sample's interaction with the 20 kV electron beam from the scanning electron microscope (SEM). Each of these spectra are discretized by the spectrometer into a 1024 energy channels, resulting in a data set which can now be considered to consist of 23,712 trials each containing 1024 recorded variables. A dataset of this many measurements does not lend itself to traditional methods developed around detailed analysis of a small number of desecrate spectra. Instead we have developed a workflow which leverages the high dimensionality of the collected data, allowing us to apply a set of machine learning algorithms to recover the four mineral phases we report.

Our workflow adapts the methods of Martineau et al.¹ and applies them directly for use on EDS data. The data is processed using opensource Python libraries^{2–4} and the final Jupyter notebook is published on Github public accessible domain (see the below Supporting Information S2). The raw spectrographic data from the Oxford Instruments is loaded offline using the Hyperspy library, where the energy and spatial dimensions are calibrated and stored in the resulting HDF5 file. We unwrap the x,y-spatial arrangement of the map to vectorize the dataset. As each energy channel (of 2048) is the variable which is being analyzed we preprocess them by centering and scaling to a component wise unit variance. Singular value decomposition (SVD), a form of principal component analysis (PCA) produces an initial dimensional reduction. The resulting components are now combinations of the 2048 energy channels, which resemble denoised EDS spectra, however, due to the mathematically pure nature of the SVD algorithm employed, these spectra possess unphysical artifacts such as negative intensities. The first three components explain 25% of the total variance in the dataset, we select these components as a new basis for exploring the data space. All the higher order components contribute 0.5% or less to the overall variance and upon inspection, can be seen to be associated with background noise. SVD performs a linear decomposition on the original EDS data, resulting in loading weights for each of the three orthogonal components which describe a new abstract dataspace. We do not present these mathematical spectra, as they do not help us understand the nature of the minerals being measured. Instead, we focus on understanding the relationships between the individual points in the data set as they are transformed by reprojection into the dataspace described by these three spectral/ component axes.

As noted above through the process of linear decomposition, SVD assigns weights to signify the amount of each of the new components contribute to the spectra measured at a single pixel in the EDS

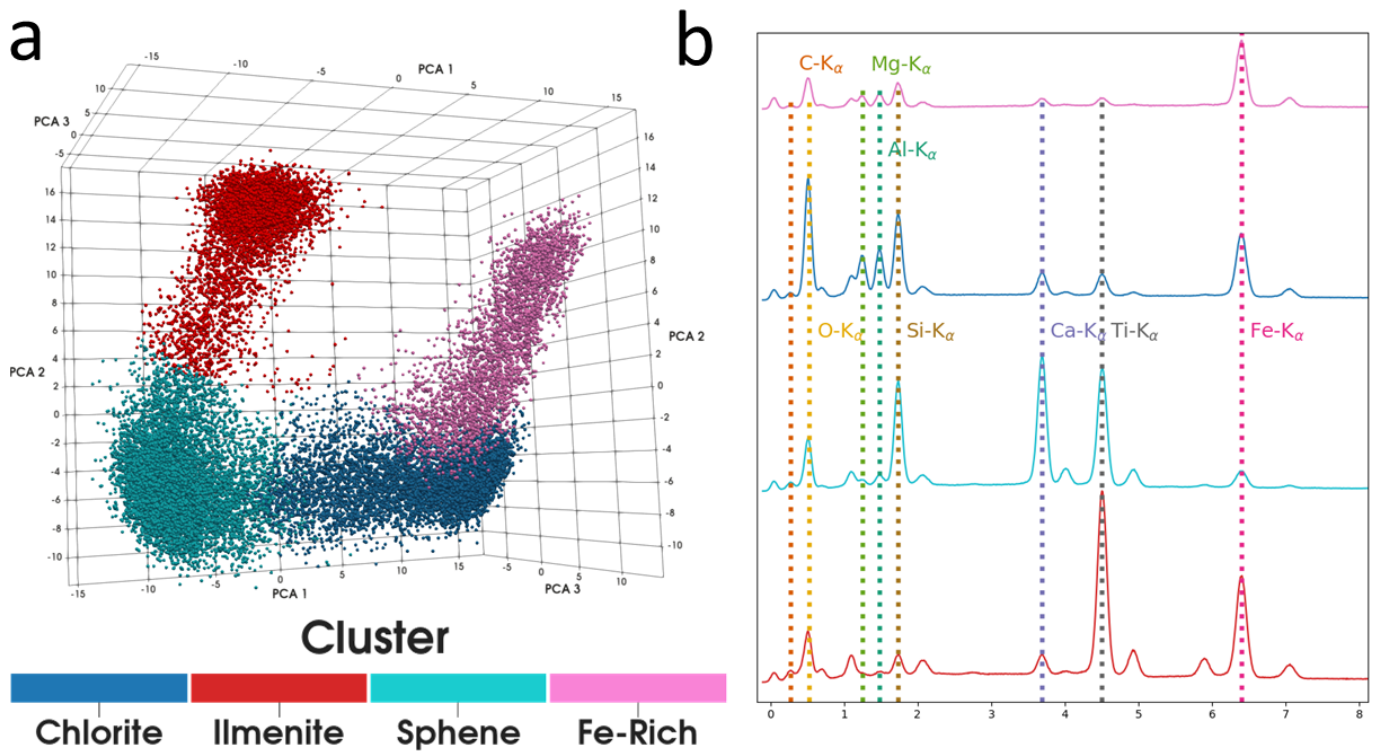
map. These weights are coordinates of each of the pixels in the resulting three-dimensional dataspace, described by first three components from the SVD analysis. By plotting out each point in the EDS data using these coordinates (Figure S1a) it is possible to see that the points form clusters. The most striking feature of examining the data points in the dataspace, is how the relationship between cluster nodes and intermediary points begin to take on a topology that from certain projections resembles a ternary phase diagram between minerals. We use a fuzzy c-means clustering algorithm to assign each point a membership in every cluster¹ which allows us to accommodate the dispersed and non-spherical nature of these clusters. Fuzzy c-means additionally has the property that a membership score of 50% or higher uniquely and non-arbitrarily associates a pixel principally with a unique cluster. Iteratively exploring the number of clusters and visual inspection of the reprojection of the membership criteria demonstrated that four clusters were the optimal to describe the minerals present in the EDS data.

Once we have assigned a cluster membership score to each point in the dataset, we reproject these scores back onto the original arrangement of the pixels. Using the 50% membership criteria to segment the membership maps produces the phase map seen in Fig 4b. We have color coded the clusters in Fig S1a to match the phase map seen in Fig 4b. Similarly, by using these membership criteria we average the spectra from the pixels which meet the membership criteria (Fig S1b). These average spectra are quantified using the Bruker software Esprit 2.0, where their implementations of the PB-ZAF and $\phi(\rho,z)$ methods. The PB-ZAF algorithm implemented in the Esprit software is a model-based method for standardless quantification, based on comparing elemental peak height to the bremsstrahlung background signal.⁵ Additionally, Esprit supports quantification using the $\phi(\rho,z)$ algorithm, using a first principles approach to model electron and x-ray interactions between multiple elements.⁶⁻⁹ Comparisons of both methods are discussed extensively in Reed (2005) and Goldstein et al (2018). The atomic percent contributions for each element measured are summarized in Table S3. We carry through the conversion into mineral formula by computing the weight percent oxide (Table S4) and using that to determine the cation balances (Table S5). The quantification differences between the two models demonstrates how the two methods account for the ZAF-correction differently. These errors are not significant since they do not affect our overall classification of the phases. We do not have evidence to classify the Fe-rich as a specific iron-oxide, so we do not carry forward any calculations of the Fe²⁺/Fe³⁺ proportions currently.

Both our sphene and chlorite spectra quantify to produce mineral formula which do not differ unexpectedly from ideal compositions. The ilmenite phase contains small amounts of Si and Ca. These likely are coming from the low-density phases that can be observed in Fig S2. Both Figs 4ai and Fig S16 demonstrate that the ilmenite grain is overgrown with sphene resulting from the seasonal weathering. We observe that this results in micro-inclusions of sphene inside the ilmenite highlighted by the orange arrows in Fig S16. Due to the beam interaction volume and overall probe size used for the EDS mapping, these low-density inclusions are only hinted at in the 20 kV BSE image collected in parallel to the EDS map (Fig S17). The beam interaction volume has several other effects besides blurring and obscuring features in a BSE image. Classical EDS analysis would suggest that in an EDS map the pixel size should not go below 1 μm in order to avoid mixing or oversampling of signals between neighboring spectra. Here we leverage the properties of machine learning to use these oversampling artifacts to reveal the weak signals associated with Fe-Oxide nanophase which are not spatially resolvable. For the cross-section surface, this allows us to highlight the presence of Fe-enrichment in the lower right corner of the surface, where the chlorite possesses a higher density of amorphous and porous weathering reaction fronts highlighted by the blue arrows in Fig S16. Due to limitations of EDS and our machine learning tools, we do not have enough information to conclude that this Fe-rich phase is magnetite, but we used magnetite as a template for determining a mineral formula for the phase.

References

- (1) Martineau, B. H.; Johnstone, D. N.; van Helvoort, A. T. J.; Midgley, P. A.; Eggeman, A. S. Unsupervised Machine Learning Applied to Scanning Precession Electron Diffraction Data. *Adv. Struct. Chem. Imaging* **2019**, *5* (1), 3. <https://doi.org/10.1186/s40679-019-0063-3>.
- (2) Peña, F. de la; Ostasevicius, T.; Fauske, V. T.; Burdet, P.; Jokubauskas, P.; Sarahan, M.; Johnstone, D.; Nord, M.; Taillon, J.; Caron, J.; et al. HyperSpy 1.1.2. January 12, 2017. <https://doi.org/10.5281/ZENODO.240660>.
- (3) Pedregosa, F.; Varoquaux, G.; Gramfort, A.; Michel, V.; Thirion, B.; Grisel, O.; Blondel, M.; Prettenhofer, P.; Weiss, R.; Dubourg, V.; et al. Scikit-Learn: Machine Learning in Python. *J. Mach. Learn. Res.* **2011**, *12* (Oct), 2825–2830.
- (4) Van Der Walt, S.; Schönberger, J. L.; Nunez-Iglesias, J.; Boulogne, F.; Warner, J. D.; Yager, N.; Gouillart, E.; Yu, T. Scikit-Image: Image Processing in Python. *PeerJ* **2014**, *2014* (1), e453. <https://doi.org/10.7717/peerj.453>.
- (5) Bruker-Nano. Introduction to EDS Analysis - Reference Manual. **2011**, 0–53.
- (6) Heinrich, K. F. J. Strategies of Electron Probe Data Reduction. In *Electron Probe Quantitation*; Springer US, 1991; pp 9–18. https://doi.org/10.1007/978-1-4899-2617-3_2.
- (7) Pouchou, J. L. X-Ray Microanalysis of Stratified Specimens. *Anal. Chim. Acta* **1993**, *283* (1), 81–97. [https://doi.org/10.1016/0003-2670\(93\)85212-3](https://doi.org/10.1016/0003-2670(93)85212-3).
- (8) Reed, S. J. B. *Electron Microprobe Analysis and Scanning Electron Microscopy in Geology*; Cambridge University Press, 2005; Vol. 9780521848756. <https://doi.org/10.1017/CBO9780511610561>.
- (9) Goldstein, J. I.; Newbury, D. E.; Michael, J. R.; Ritchie, N. W. M.; Scott, J. H. J.; Joy, D. C. *Scanning Electron Microscopy and Microanalysis*, 4th ed.; Springer, 2018. https://doi.org/10.1007/978-1-4684-2046-3_11.



S15 (a) projection of the EDS data into the three-dimensional data space described by three principal components. Points are colored by membership in one of four clusters. These have been named based on EDS quantification. (b) Average phase spectra extracted from EDS map based on membership criteria.

S2. We push the python code and documentation via Github public access domain:
https://github.com/MAG-tominaga/GRL_SupportingInfo_S2_ForReviewers

https://github.com/MAG-tominaga/GRL_SupportingInfo_S2_ForReviewers Private

Unwatch 1 ★ Star 0 Fork 0

Code Issues 0 Pull requests 0 Actions Projects 0 Security 0 Insights Settings

This is the Supporting Info S2 for GRL reviewers' view Edit

Manage topics

1 commit 1 branch 0 packages 0 releases

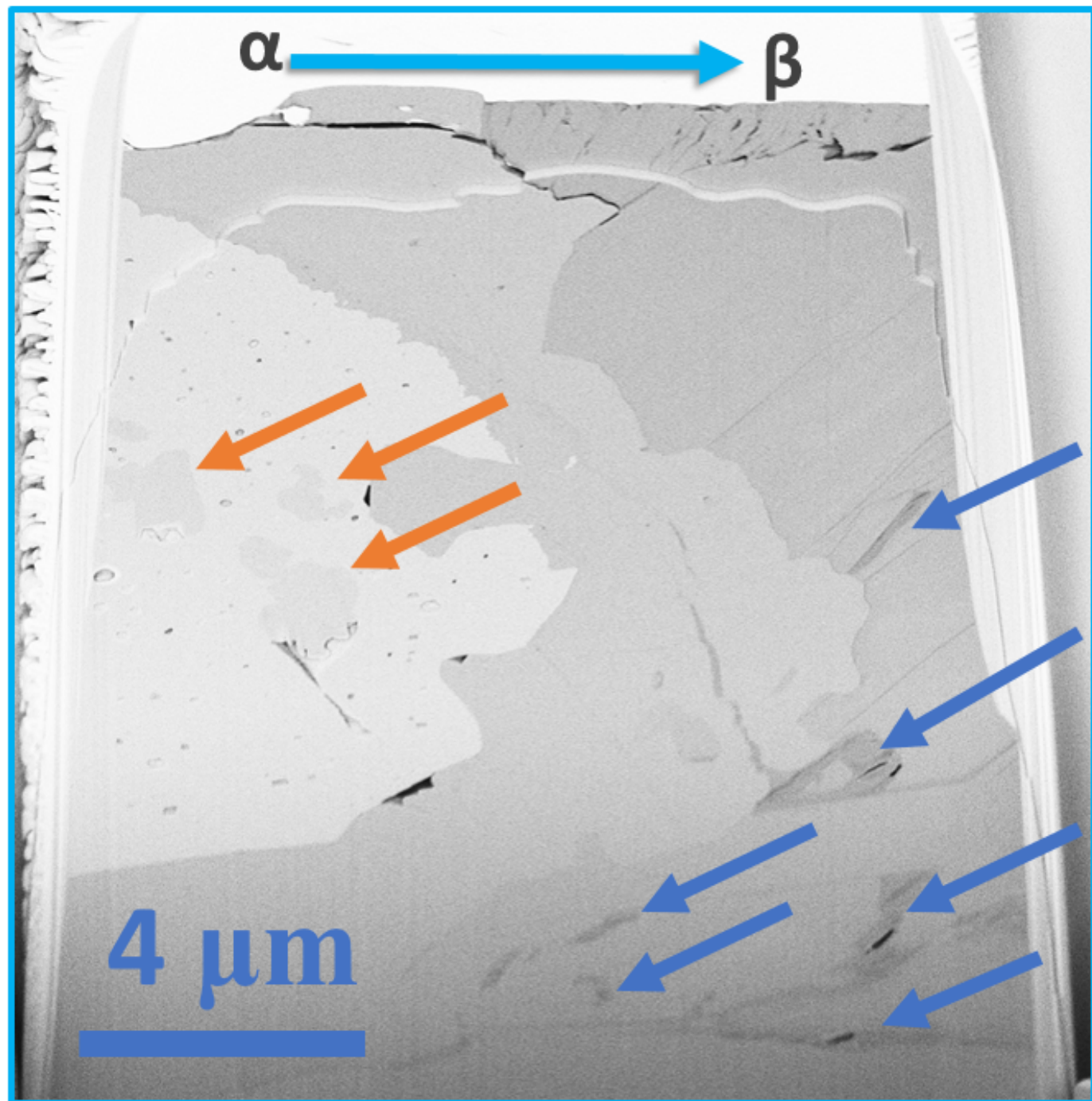
Branch: master New pull request Create new file Upload files Find file Clone or download

MAG-tominaga Add files via upload Latest commit ac22b3e 2 minutes ago

QV1.120_xs_roi2_EDS_Cluster_annotated_rev3.ipynb Add files via upload 2 minutes ago

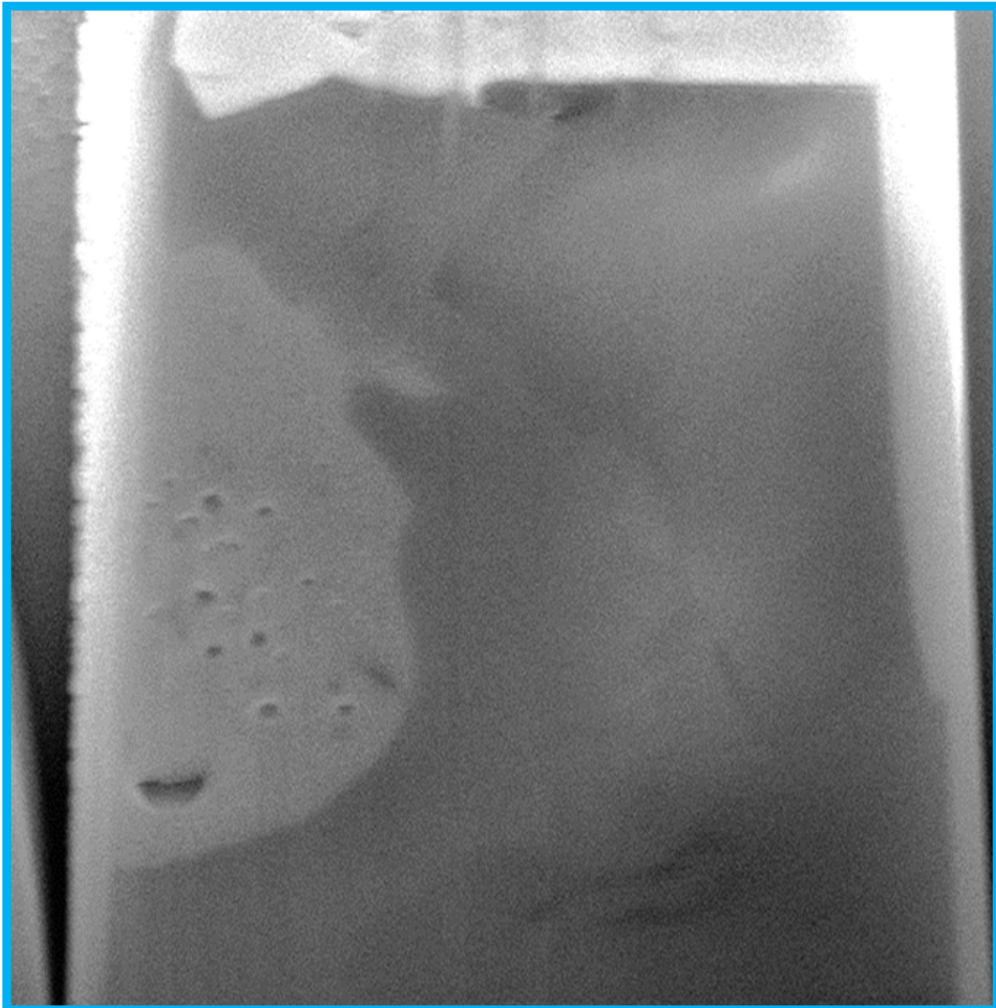
QV1.120_xs_roi2_EDS_Cluster_annotated_rev3.pdf Add files via upload 2 minutes ago

Add a README with an overview of your project. Add a README



S16 3 kV BSE image of Oxide-Chlorite interface. Full resolution reproduction of Fig 4c. Dark blue arrows have been added to highlight low density reaction fronts lacing through the chlorite. There is a higher density of these features towards the bottom of the cross section surface compared to the top. Orange arrows highlight lower density phases in the Rutile grain. Additionally, the rutile grain possess a large volume of porosity which is apparent in this BSE image.

α → β



4 μm

S17 20 kV BSE image of cross section face (17 nm pixel size).

Compositional Tables

Table S1. Reduced Mineral list QEMScan modal mineralogy based on individual pixel classifications or each of the QV samples. Percentages calculated on total measured pixels. Used to generate categories in for Figs S1-S5.

Sample	QV1.17	QV1.20		
Mineral Classification	no. of pixels	% fraction	no. of pixels	% fraction
Serpentine	447	0.049	92335	4.387
Chlorite	63326	6.967	600393	28.523
Olivine	852	0.094	235350	11.181
Talc	2360	0.260	42039	1.997
Sphene	2581	0.284	5646	0.268
Magnetite\Hematite	0	0.000	0	0.000
Cr-Spinel	36	0.004	2673	0.127
Goethite/limonite	1091	0.120	388	0.018
Rutile/Anatase	4	0.000	48	0.002
Total	11111	11111	11111	11111

Table S2. Comprehensive QEMScan modal mineralogy based on individual pixel classifications or each of the QV samples. Percentages calculated on total measured pixels. These categories are used to generate Figures S6-S10.

Sample	QV1.17	QV1.20	QV1.2			
Mineral Classification	no. of pixels	% fraction	no. of pixels	% fraction	no. of pixels	%
Serpentine	442	0.058	91548	6.447	304407	
Chlorite	63326	8.276	600393	42.280	120716	
Augite	46710	6.104	380978	26.828	202871	
Olivine	852	0.111	235350	16.573	159034	
Glass/mesostasis	224340	29.318	--	--	--	
Plagioclase	160799	21.014	--	--	8470	
Biotite/Phlogopite	137378	17.953	--	--	2846	
Amphibole	31591	4.128	56304	3.965	20487	
Talc	2360	0.308	42039	2.960	30471	
Quartz	40551	5.299	201	0.014	8059	
K-Feldspar	40610	5.307	--	--	329	
Calcite	63	0.008	2406	0.169	35668	
Magnetite\Hematite	--	--	--	--	--	
Garnet	6431	0.840	691	0.049	1889	
Cr-Spinel	38	0.005	2673	0.188	6320	
Goethite/limonite	1091	0.143	388	0.027	203	
Sphene	2581	0.337	5646	0.398	1317	
Pyrite	2266	0.296	--	--	253	
Muscovite	2232	0.292	--	--	122	
Apatite	635	0.083	1221	0.086	255	
Epidote	754	0.099	--	--	140	

Table S3. QEMScan Relative Fe weight percent estimates for the QV well samples based on pixel data.

	QV 1.17	QV 1.20	QV 1.27	QV 1.23	QV 1.37
Fe:<2%	0	0	0	0	0
Fe:2-5%	16.884	3.247	2.627	2.627	31.218
Fe:5%	7.91	4.754	2.438	2.438	26.553
Fe:6%	8.608	8.261	4.589	4.589	20.591
Fe:7%	8.593	11.478	7.563	7.563	10.566
Fe:8%	7.797	13.808	10.971	10.971	3.973
Fe:9%	6.704	14.777	13.587	13.587	1.289
Fe:10%	19.335	37.254	45.967	45.967	0.951
Fe:15%	7.979	3.323	5.471	5.471	0.249
Fe:20%	3.468	0.997	1.111	1.111	0.146
Fe:25%	1.896	0.425	0.35	0.35	0.119
Fe:30%	1.202	0.202	0.14	0.14	0.089
Fe:35%	0.63	0.098	0.06	0.06	0.084
Fe:40%	0.144	0.047	0.032	0.032	0.069
Fe:>45%	0.091	0.102	0.072	0.072	2.411
Others	8.76	1.228	5.022	5.022	1.693

Tables S4 Normalized Elemental Atomic percentages. Standardless EDS quantification was calculated using the Bruker ESPRIT 2.0 software, and applying both their P/B-ZAF-Oxides algorithm and the $\phi(\rho,z)$ methods.

element	Normalised EDS Atomic Percent					
	Chlorite		Ilmenite		Fe-rich	
	P/B-ZAF	$\Phi(\rho,z)$	P/B-ZAF	$\Phi(\rho,z)$	P/B-ZAF	$\Phi(\rho,z)$
Si	10.06	8.53	1.46	1.77	1.46	7.36
Ti	2.84	2.63	20.11	18.74	20.11	1.99
Al	6.79	5.05	0.00	0.00	0.00	4.57
Fe	11.23	14.11	14.02	18.90	14.02	30.49
Mg	7.69	5.55	0.00	0.35	0.00	5.93
Mn	0.13	0.29	1.90	3.10	1.90	0.49

Table S5 Weight Percent Oxides. Atomic percentages were used to determine oxide weight percentages, based on assumed mineral ids. For Fe-rich phase, this was compared against magnetite.

Oxide	Weight Pe		
	Chlorite		
	P/B-ZAF	$\Phi(\rho,z)$	Norm
SiO ₂	30.38	20.30	21.3
TiO ₂	6.69	8.31	8.8
Al ₂ O ₃	18.13	10.21	10.3
FeO	20.40	40.17	42.0
MgO	18.00	8.87	9.3
MnO	0.23	0.80	0.8
CaO	6.17	5.72	6.0
sum	100.00	94.38	100

Table S6 Mineral stoichiometry. Weight percent oxides (S4) are used to compare against accepted stoichiometries for assumed mineral ids. Fe-rich phase was compared against magnetite as reference iron oxide.

Stoichiometry			
Oxide	Chlorite		
	P/B-ZAF	$\Phi(\rho,z)$	P/B-
	Cations per 12 oxygen atoms	Cations	
Si	4.84	4.56	
Ti	1.37	1.40	
Al	3.27	2.70	
Fe	5.41	7.54	
Mg	3.70	2.97	
Mn	0.06	0.15	
Ca	1.50	1.38	
Cation sum	20.15	20.69	
Stoichiometry			
Oxide	Fe-rich		
	P/B-ZAF	$\Phi(\rho,z)$	P/B-
	Cations per 32 oxygen atoms	Cations	
Si	4.86	3.66	
Ti	0.99	0.99	